Journal of the Taiwan Institute of Chemical Engineers xxx (xxxx) xxx

Contents lists available at ScienceDirect

Journal of the Taiwan Institute of Chemical Engineers

journal homepage: www.journals.elsevier.com/journal-of-the-taiwan-institute-of-chemical-engineers

Benzoxazine-linked polyhedral oligomeric silsesquioxane: 3D porous organic-inorganic polymer for improved CO_2 capture and supercapacitor performance

Mohsin Ejaz [a], Mohamed Gamal Mohamed [a,b,*], Shiao-Wei Kuo [a,c,*]

[a] Department of Materials and Optoelectronic Science, Center for Functional Polymers and Supramolecular Materials, National Sun Yat-Sen University, Kaohsiung 804, Taiwan
[b] Chemistry Department, Faculty of Science, Assiut University, Assiut 71515, Egypt
[c] Department of Medicinal and Applied Chemistry, Kaohsiung Medical University, Kaohsiung 807, Taiwan

ARTICLE INFO

Keywords:
Porous organic-inorganic polymer
Benzoxazine
POSS
CO_2 capture
Supercapacitor

ABSTRACT

Background: Three-dimensional (3D) porous organic polymers (POPs) are known for high surface areas, customizable porous architectures, and remarkable durability, making them highly attractive for energy storage, catalysis, gas separation, and environmental remediation applications. Despite significant advancements in the field, synthesizing benzoxazine-based 3D porous organic polymers incorporating octavinyl polyhedral oligomeric silsesquioxane (OVS) remains unexplored.

Methods: In this study, we present the synthesis of a novel 3D benzoxazine-linked porous organic-inorganic polymer (OVS-DHBZ POIP) through a Heck coupling reaction between a brominated benzoxazine monomer (DHBZ-Br_2) and OVS. The chemical structures of DHBZ-Br_2 and the resulting OVS-DHBZ POIP were confirmed using ^1H and ^{13}C NMR, and FTIR spectroscopy.

Significant Findings: The specific surface area (S_{BET}) of OVS-DHBZ POIP, determined via N_2 adsorption/desorption isotherms, was 690 $m^2\ g^{-1}$. After undergoing solid-state ring-opening polymerization (ROP), the poly(OVS-DHBZ POIP) displayed an increased S_{BET} of 762 $m^2\ g^{-1}$. Thermal stability analysis revealed that poly(OVS-DHBZ POIP) exhibited a significantly enhanced decomposition temperature (T_{d10}) of 665 °C with a char yield of 86 wt%, setting a benchmark for benzoxazine-based POPs in terms of surface area and thermal stability. Moreover, poly (OVS-DHBZ POIP) demonstrated impressive CO_2 capture capabilities, with adsorption capacities of 1.03 mmol g^{-1} at 298 K and 1.68 mmol g^{-1} at 273 K. When evaluated supercapacitor performance, the material achieved a specific capacitance of 58 F g^{-1}. The outstanding properties of poly(OVS-DHBZ POIP) can be attributed to phenolic groups and Mannich bridges, which facilitate robust intra- and intermolecular hydrogen bonding. These interactions contribute to its enhanced surface area, exceptional thermal stability, and superior electrochemical and CO_2 capture performance. This study underscores the potential of poly(OVS-DHBZ POIP) as a multifunctional material for advanced energy storage systems and sustainable CO_2 capture technologies.

1. Introduction

Porous organic polymers (POPs) are intriguing materials due to their distinctive characteristics, which include high thermal stability, exceptional chemical resilience, efficient energy regeneration, lightweight, convenient synthesis, ease of modification, and variable porosity [1–4] . These attractive materials have been employed in various applications, like dye adsorption and degradation, gas capture, batteries, photocatalysis, electrocatalysis, fluorescence sensors, water splitting, supercapacitors, CO_2 capture and conversion [5–10].

Organic-inorganic compounds are considered sophisticated, novel substances that provide a compelling study area. A conventional hybrid material comprises a crosslinked inorganic phase covalently bonded to an organic phase. The characteristics of the hybrid material may be regulated by the proportional quantities of its constituents. Currently, hybrid porous polymers derived from polyhedral oligomeric silsesquioxanes (POSS) have been extensively prepared and utilized in water treatment, iodine capture, energy storage, chemical sensing, hydrogen

* Corresponding authors.
E-mail addresses: mgamal.eldin12@aun.edu.eg (M.G. Mohamed), kuosw@faculty.nsysu.edu.tw (S.-W. Kuo).

https://doi.org/10.1016/j.jtice.2025.106098
Received 10 December 2024; Received in revised form 22 February 2025; Accepted 12 March 2025

evolution, and many other applications [11–17]. Octavinylsilsesquioxane (OVS) is a type of silsesquioxane cage with a diameter ranging from 1 to 3 nm. Numerous instances of porous polymer developed by incorporating OVS as a basic framework, featuring a high porosity, exceptional thermal durability, and adjustable shape have been documented and executed by several research groups by the Heck coupling reaction [18–21]. There is a significant need for efficient, affordable, eco-friendly energy storage systems, driven by the growth in the manufacture of power and electronic industries. For advanced energy storage systems, key requirements include high power and energy density, exceptional safety, the use of abundant materials, and long-term durability. Supercapacitors, distinguished by their high-power density, exceptional safety, and longevity exceeding 10^6 cycles, are relatively low-cost energy storage devices. However, their lower energy density (<10 Wh kg^{-1}) compared to batteries significantly restricts their applications [22–26].

Benzoxazines (BZs) constitute a novel category of thermosetting materials capable of establishing hydrogen bonding following the ring opening of the oxazine group and are extensively utilized in many applications [27–31]. Benzoxazine monomers are typically synthesized through the Mannich reaction [32,33]. A new approach for synthesizing benzoxazine-linked POPs (BZ-POPs) emphasizes their potential for achieving large surface areas. The benefits of functionality integration and high surface area modification enhance the potential for customized applications. We synthesized a fully BZ-POP with S_{BET} of 195 m^2 g^{-1} through the Sonogashira coupling of brominated benzoxazine and ethylene benzoxazine [34]. Tan et al. prepared three BZ-POPs through the Mannich process, achieved surface areas above 230 m^2 g^{-1} [35]. In another study, we designed TPE-BZ CMP with high S_{BET} (352 m^2 g^{-1}) [36]. Nonetheless, the documented studies only used two-dimensional (2D) BZ-POPs, whereby the planar sheets were generally arranged in a face-to-face configuration, leading to pronounced π-π interactions. However, 3D POPs provide many accessible sites and pore confinement effects, potentially resulting in improved catalysis and adsorption efficacy. Sun et al. prepared two BZ-POPs that experienced a high surface area surpassing 630 m^2 g^{-1} [37]. We prepared 3D tetrahedral BZ-POP that exhibited a surface area of 185 m^2 g^{-1} [38]. However, 3D benzoxazine linked with OVS to afford highly porous organic-inorganic polymer (POIP) has not been reported yet.

Herein, we successfully synthesized a three-dimensional (3D) benzoxazine (BZ)-linked octavinyl-polyhedral oligomeric silsesquioxane POIP through a Heck coupling reaction. The process began with the synthesis of DHBZ via a Mannich reaction involving bis(2,4-dihydroxybenzylidene)hydrazine [DHBH-4OH], 4-bromoaniline, and paraformaldehyde. Subsequently, 3D BZ-linked POIPs were constructed by the Heck coupling of DHBZ-Br_2 with OVS building blocks, yielding the 3D OVS-DHBZ POIP. The newly developed 3D OVS-DHBZ POIP undergoes ROP, resulting in the formation of phenolic hydroxyl (OH) units and Mannich bridges. These transformations enhance the material's thermal stability, porosity, CO_2 capture capacity, and supercapacitor performance. According to our understanding, the design and synthesis of a 3D benzoxazine-linked POIP utilizing OVS as a structural component was never discussed before. This rational design approach offers a novel and versatile pathway for advancing the development of porous organic-inorganic polymers with tailored functionalities for diverse applications.

2. Experimental section

2.1. Materials

4-Bromoaniline, methanol (MeOH), paraformaldehyde (96 %), 1,4-dioxane (DO), tetrahydrofuran (THF), 2,4-dihydroxybenzaldehyde (CHO-BZ-2OH), acetone, and DMF were provided by Acros. Hydrazine monohydrate (98 %), ethanol, and 1,4-dioxane were used as received from Alfa Aesar. Potassium carbonate (K_2CO_3), OVS, and tetrakis (triphenylphosphine) palladium (0) [$Pd(PPh_3)_4$] were bought from Sigma-Aldrich.

2.2. Synthesis of bis(2,4-Dihydroxybenzylidene)hydrazine (DHBH-4OH)

The CHO-BZ-2OH (4.00 g, 28.9 mmol) and hydrazine monohydrate (0.73 g, 14.5 mmol) were dissolved in 90 mL of EtOH. Following a night of stirring at 25 °C, the yellow precipitate was collected and washed with EtOH (Yield: 88 %) [**Figure S1**] [39]. FTIR (KBr, cm^{-1}): 3240–3450 (OH stretching), 1640 (C═N). ^{1}H NMR (δ, ppm): 11.36 (OH), 10.18 (OH), 8.73 (C═N), 7.4 (C═C), 6.44 (C═C), 6.27 (C═C). ^{13}C NMR (δ, ppm): 163.2 (OH), 161.4 (OH), 133.50 (C═N), 111 (C═C), 108.8 (C═C), 102.6 (C═C).

2.3. Synthesis of benzoxazine monomer (DHBZ-Br_2)

40 mL of 1,4-dioxane, 20 mL of ethanol, 0.7 g of DHBH (2.5 mmol), 0.97 g of 4-bromoaniline (5.6 mmol), and 0.32 g of paraformaldehyde were added. A reflux heater set to 80 °C was used to heat the reaction mixture for 24 h. A yellow solid was obtained by evaporating the solvent under reduced pressure. The resulting solid was then dissolved in ethyl acetate and subjected to extraction with 1 N NaOH. After removing ethyl acetate, pure DHBZ-Br_2 was obtained (yield: 88 wt.%) [Fig. 1(a)]. FTIR (KBr, cm^{-1}): 3400–3250 (OH stretching), 942, and 1060 (oxazine ring and C—O-C) [Fig. 1(b)]. ^{1}H NMR (δ, ppm): 12.02 (OH), 8.90 (C═N), 7.46–6.6 (CH aromatics), 5.52 (O–CH_2–N), and 4.58 (Ar-CH_2–N) [Fig. 1 (c)]. ^{13}C NMR (δ, ppm): 164.6 (stable OH), 157.8 (C═N), 147–108 (CH aromatics), 79.62 and 45.64 [Fig. 1(d)].

2.4. Synthesis of OVS-DHBZ POIP

In a 50 mL flask, a combination of OVS (0.1 g, 0.15 mmol), DHBZ-Br_2 (0.42 g, 0.63 mmol), anhydrous K_2CO_3 (0.25 g, 2.5 mmol), and Pd $(PPh_3)_4$ (0.0073 g, 0.006 mmol) and DMF (30mL) were added. The mixture underwent three cycles of freezing, evacuating, and thawing to remove oxygen and finally heated under reflux for 96 h at 120 °C with N_2. The OVS-DHBZ POIP (a light-yellow powder with a 60 wt.% yield) was obtained by opening the tube, filtering off the precipitate, washing with MeOH, acetone, and THF by Soxhlet extraction, and finally drying in an oven after it had cooled to room temperature [Fig. 3(a)].

3. Result and discussion

3.1. Synthesis and thermal ROP behavior of DHBZ-Br_2

The synthesis of DHBZ-Br_2 was achieved through a Mannich condensation reaction involving DHBH-4OH, 4-bromoaniline, and paraformaldehyde at 100 °C for 24 h [Fig. 1**(a)**]. The chemical structure of the synthesized compound was elucidated using FTIR and NMR spectroscopy. The FTIR spectrum of DHBH-4OH revealed characteristic peaks at 3240–3450 cm^{-1} and 1640 cm^{-1}, corresponding to the stretching vibrations of free and stable OH groups and the C═N bond, respectively [Fig. 1**(b)**].

In comparison, DHBZ-Br_2 exhibited distinct signals at 3400–3250 cm^{-1} (OH), 1060 cm^{-1} (benzoxazine ring), and 942 cm^{-1} (symmetric C–O–C), indicating the successful formation of the benzoxazine structure [Fig. 1**(b)**]. The ^{1}H NMR spectra provided further confirmation. DHBH-4OH displayed signals at 11.36 ppm (stable OH), 10.18 ppm (free OH), 8.73 ppm (C═N), and aromatic peaks at 7.4 ppm, 6.44 ppm, and 6.27 ppm (C═C). Following the Mannich reaction, the ^{1}H NMR signal of DHBZ-Br_2 exhibited new signals at 12.02 ppm (stable OH), 8.90 ppm (C═N), and 5.52 ppm (O–CH_2–N), along with peaks at 4.58 ppm (Ar–CH_2–N) and 7.46–6.6 ppm (aromatic CH) [Fig. 1**(c)**]. Similarly, the ^{13}C NMR spectra validated the findings of FTIR and ^{1}H NMR analyses. Peaks observed for DHBH-4OH included signals at 163.2 ppm (stable OH), 161.4 ppm (free OH), 133.5 ppm (C═N), and 111–102.6 ppm

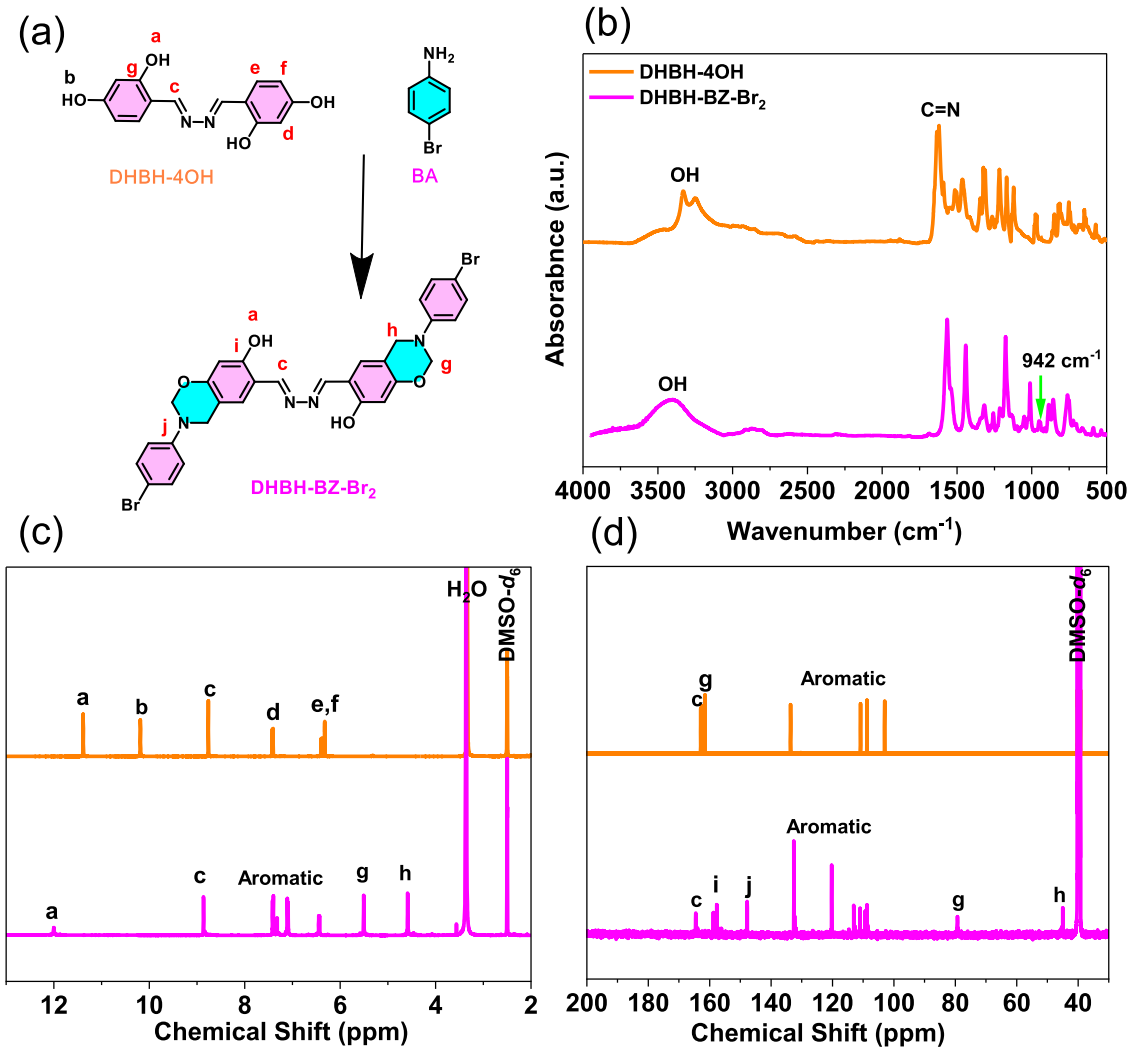

Fig. 1. (a) Synthesis of DHBZ-Br_2 monomer (b) FTIR, (c) ^{1}H NMR, and (d) ^{13}C NMR spectra of DHBH and DHBZ-Br_2.

(aromatic C═C). After the Mannich condensation reaction, the spectrum of DHBZ-Br_2 featured peaks at 164.6 ppm (phenolic OH), 157.8 ppm (C═N), 147–108 ppm (aromatic CH), 79.62 ppm (O–CH_2–N), and 45.64 ppm (Ar–CH_2–N) [Fig. 1**(d)**]. The disappearance of the free OH group and the emergence of benzoxazine-specific peaks across FTIR, ^{1}H NMR, and ^{13}C NMR analyses unequivocally confirm the successful synthesis of the benzoxazine monomer, DHBZ-Br_2. These results establish the molecular structure and validate the Mannich condensation as an efficient pathway for preparing functional benzoxazine-based materials. The ROP behavior of the DHBZ-Br_2 monomer was studied using DSC, FTIR spectroscopy, and TGA at room temperature and 250 °C. The DSC thermogram confirmed the high purity of the brominated benzoxazine monomer, displaying a prominent exothermic peak at 222 °C [Fig. 2(a)]. Notably, no additional thermal polymerization peaks were observed after heat treatment at 250 °C, suggesting the complete ROP at this temperature [Fig. 2**(a)**]. To further elucidate the structural changes during thermal polymerization, in situ FTIR spectroscopy was conducted at various temperatures [Fig. 2**(b)**]. The peaks at 942 cm^{-1} and 1060 cm^{-1}, representing the oxazine ring and symmetric C–O–C stretching, respectively, disappeared completely after heat treatment.

This disappearance confirmed the completion of ROP and the formation of a cross-linked, thermally stable poly(DHBZ-Br_2) network [Fig. 2**(b)**]. TGA analysis provided insights into the thermal stability of DHBZ-Br_2, focusing on the 10 wt.% degradation temperature (T_{d10}) and char yield. Before thermal curing, the T_{d10} and char yield of DHBZ-Br_2 were 253 °C and 37 wt%, respectively. After thermal ROP, these values increased to 380 °C and 43 wt.% [Fig. 2**(c)**]. The enhanced thermal stability is attributed to the thermal ROP of the oxazine rings, which facilitated the development of a highly cross-linked poly(DHBZ-Br_2) structure [Fig. 2**(d)**]. The cross-linking, combined with intra- (O–H···N) and intermolecular hydrogen bonding (O–H···O), significantly improved the thermal stability of the polybenzoxazine. Differential thermogravimetric (DTG) analysis was conducted to gain deeper insight into the thermal degradation behavior, as illustrated in **Figure S2**. The derivative weight loss curve of DHBZ-Br_2 exhibited two distinct decomposition stages. The first peak, observed at 248 °C, corresponds to the ROP of the oxazine ring, while the second peak, occurring at approximately 405 °C, represents the complete degradation of DHBZ-Br_2. In contrast, the complete degradation of the poly(DHBZ-Br_2) backbone took place at around 406 °C.

3.2. *Synthesis and thermal ROP behavior of 3D OVS-DHBZ POIP*

The 3D OVS-DHBZ POIP was successfully prepared through a Heck reaction between DHBZ-Br_2 and OVS at 90 °C for 3 days [Fig. 3**(a)**]. The structural characteristics and thermal ROP behavior of the resulting 3D OVS-DHBZ POIP were analyzed using FTIR, NMR, and DSC techniques. The FTIR spectrum of OVS displayed a distinct absorption band at 1059 cm^{-1}, corresponding to the Si-O-Si unit [Fig. 3**(b)**]. In addition, the FTIR spectrum of the 3D OVS-DHBZ POIP exhibited key absorption bands at

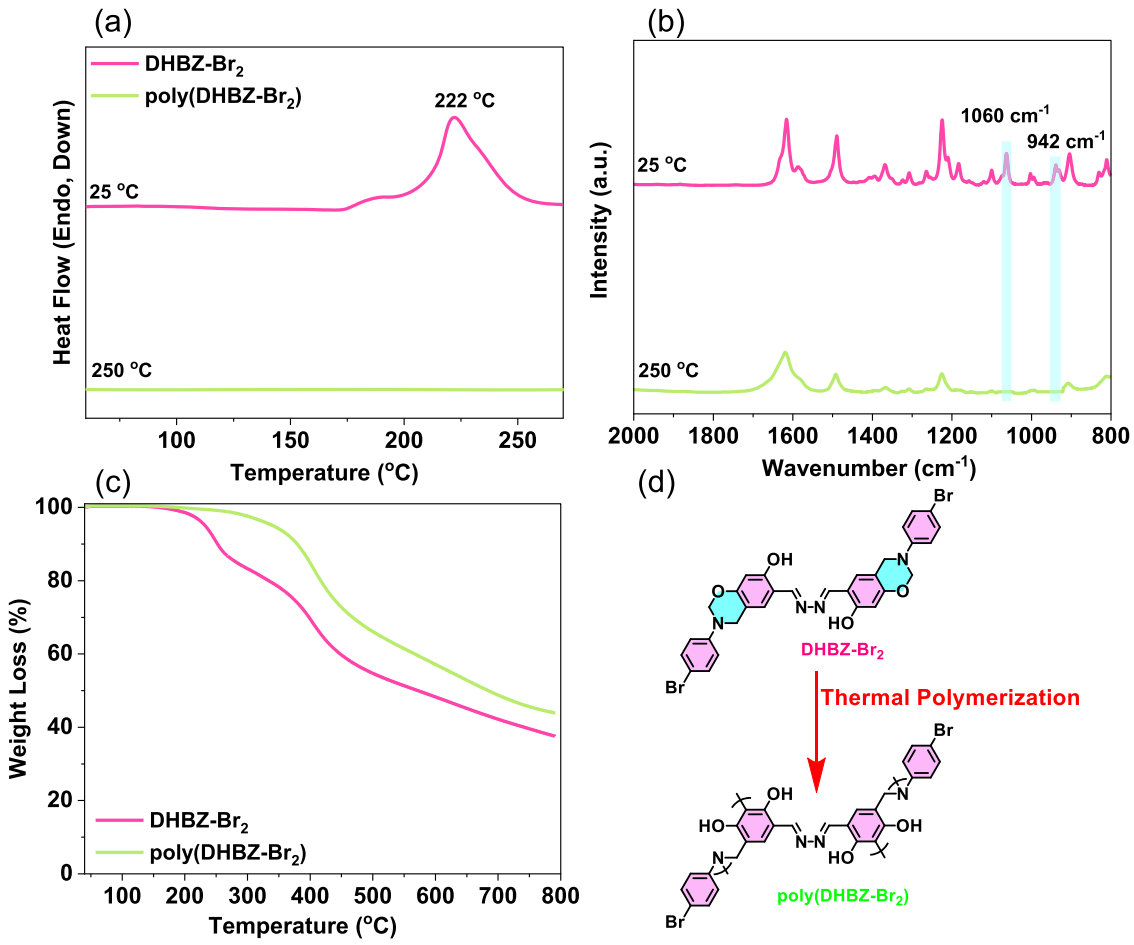

Fig. 2. (a) DSC, (b) FTIR spectra, (c) TGA analyses, and (d) possible ROP of DHBZ-Br_2 monomer before and after thermal polymerization.

1647 cm^{-1} (C═C stretching), 1160–1030 cm^{-1} (Si–O–Si stretching), and 964 cm^{-1} (oxazine ring), confirming the successful formation of the polymer [Fig. 3**(b)**]. As shown in Fig. 3**(c)**, the OVS molecule exhibits two distinct carbon resonance signals at 137.4 ppm and 128.1 ppm, corresponding to the C═C groups. Solid-state ^{13}C NMR spectroscopy further validated the structural features, with peaks observed at 154 ppm (C—OH), 146–122 ppm (aromatic carbons), 72.0 ppm (O–CH_2–N), and 30.6 ppm (Ar–CH_2–N) [Fig. 3**(c)**]. The presence of the oxazine ring signal was indicative of the successful synthesis and incorporation of the DHBZ-Br_2 moieties within the polymer framework.

Thermal stability and crosslinking of the 3D OVS-DHBZ POIP were evaluated using TGA. The thermal degradation properties of the monomers (OVS and DHBZ-Br_2) were assessed individually and compared to the resulting polymer. The OVS monomer displayed a T_{d10} of 254 °C and a char yield of 3.6 wt.%, whereas DHBZ-Br_2 exhibited a T_{d10} of 252 °C and a char yield of 37 wt.%. Notably, after the Heck reaction and formation of the 3D OVS-DHBZ POIP, the polymer demonstrated significantly enhanced thermal stability, with a T_{d10} of 627 °C and a char yield of 84 wt.% [Fig. 3**(d)**]. The significant enhancement in thermal stability compared to the monomers suggests the formation of a highly crosslinked polymer network. The thermal ROP behavior of the 3D OVS-DHBZ POIP was systematically analyzed using DSC, solid-state ^{13}C NMR, and TGA at room temperature and 250 °C [Fig. 4]. DSC analysis conducted at room temperature revealed a broad exothermic peak centered at 232 °C, indicative of the ROP process. Notably, this exothermic peak was absent at 250 °C, confirming the completion of the ROP at this elevated temperature [Fig. 4**(a)**]. This observation aligns with the successful polymerization of oxazine rings, which facilitates the formation of a robust, thermally stable, crosslinked network within the 3D OVS-DHBZ POIP. The polymerization process of the 3D OVS-DHBZ POIP was further corroborated by solid-state ^{13}C NMR analysis. At room temperature, the characteristic peaks appeared at 72.0 ppm (representing to O–CH_2–N) and 30.6 ppm (assigned to Ar–CH_2–N), verifying that the oxazine ring is present. Upon heating to 250 °C, these peaks disappeared entirely, indicating the complete ring-opening of the oxazine groups and the successful progression of the ROP [Fig. 4**(b)**]. TGA was employed to evaluate the thermal stability of the material before and after ROP [Fig. 4**(c)**]. The uncured OVS-DHBZ POIP exhibited a T_{d10} of 627 °C and a char yield of 84 wt.%. After thermal ROP, these values enhanced to 665 °C and 85 wt.%, respectively, as shown in [Fig. 4**(d)**]. This enhancement in thermal stability, coupled with the disappearance of oxazine ring signals, strongly indicates the development of a highly crosslinked framework during the thermal ROP process.

The ROP of 3D OVS-DHBZ POIP into a highly crosslinked 3D poly (OVS-DHBZ POIP) is schematically illustrated in Fig. 5, emphasizing the structural evolution and robust network formation.

3.3. Porosity and morphology OF OVS-DHBZ POIP and poly(OVS-DHBZ POIP)

To assess the porosity of 3D OVS-DHBZ POIP, N_2 adsorption/desorption isotherms were recorded at 77 K [Fig. 6]. A significant increase in N_2 adsorption at low pressures ($P/P_o < 0.1$) indicates strong van der Waals interactions with nitrogen molecules and the OVS-DHBZ POIP framework. At relatively higher pressure, rapid nitrogen uptake suggests That there is a mesoporous structure [Fig. 6**(a)**]. Based on the IUPAC classification, the adsorption-desorption isotherm corresponds to a Type IV isotherm. The OVS-DHBZ POIP has S_{BET} of 690 m^2/g, a total

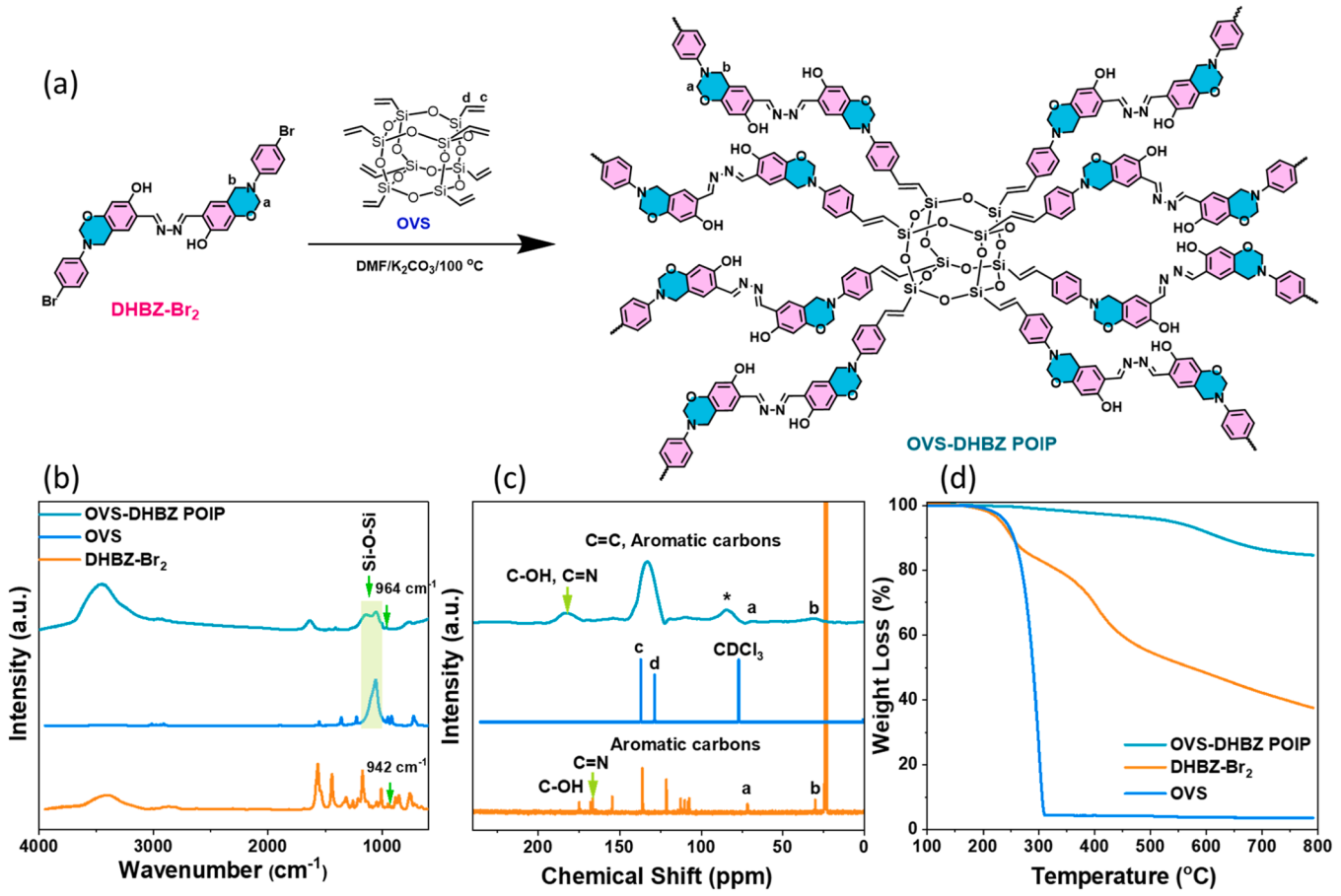

Fig. 3. (a) Synthesis of OVS-DHBZ POIP, (b) FTIR, (c) SS ^{13}C NMR, and (d) TGA spectra of OVS, DHBZ-Br$_2$ and OVS-DHBZ POIP.

pore volume (V_{total}) of 1.98 cm^3/g, and an average pore size of 2.15 nm [Fig. 6**(c)**]. After undergoing thermal ROP, the poly(OVS-DHBZ POIP) exhibited an enhanced S_{BET} of 762 m^2/g, V_{total} of 2.3 cm^3/g, and an average pore size of 2.24 nm [Fig. 6**(b) and (d)**].

Notably, our synthesized BZ POIPs exhibits the highest surface area reported among benzoxazine-based porous organic polymers such as 3D TPM-BZ-Py (185 m^2/g) [38], TPA–DHTP–BZ POP (195 m^2/g) [39], BoxPOP-1 (231 m^2/g) [35], TPE-BZ CMP (352 m^2/g) [36], Py-TPE-BZ CMP (301 m^2/g) [36], CE-BZ-Py POP (11.9 m^2/g) [40], Cr-TPA-4BZ-Py-POP (2.27 m^2/g) [41], and Pery-DHTP-BZ-COP (25 m^2/g) [42]. The increase in surface area of poly(OVS-DHBZ POIP) can be attributed to several key factors: (1) high 3D cross-linked framework: the thermal ROP of benzoxazines leads to the formation of a cross-linked network. Incorporating POSS into this system enhances cross-linking due to its silsesquioxane structure, increasing the number of connection points within the polymer matrix. This higher cross-linking density promotes the development of a more intricate three-dimensional structure, resulting in a larger surface area as the material expands [43] and (2) hydrogen bonding may influence the degree of crosslinking, pore formation, increasing thermal stability, and encouraging supramolecular interactions in polybenzoxazines. Strong hydrogen bonds, especially those between hydroxyl (OH) groups and nitrogen atoms, may prevent excessive cross-linking by stabilizing structures, resulting in decreased cross-link density [44]. This might result in larger voids and higher porosity inside the material. The morphology of OVS-DHBZ POIP before and after ROP was analyzed by TEM and SEM images with their corresponding C, N, O, and Si mapping [Fig. 7]. The SEM images of both POIPs showed aggregated spherical clusters of nanoparticles. The TEM images of POIPs also demonstrated spherical particles with porous structures.

3.4. CO_2 capture performance of OVS-DHBZ POIP and poly(OVS-DHBZ POIP)

The thermal ROP of OVS-DHBZ POIP induced a chemical transformation that generated phenolic groups and Mannich bridges which facilitate robust intermolecular interactions with guest molecules, suggesting significant potential for CO_2 capture due to the enhanced chemical functionality and high surface area. To explore this application, CO_2 capture analysis was conducted at 298 K and 273 K under 1 bar pressure [Fig. 8]. The results revealed that the CO_2 capture capacity of uncured OVS-DHBZ POIP was 0.69 mmol g^{-1} at 298 K [Fig. 8**(a)**] and 1.18 mmol g^{-1} at 273 K. Following thermal ROP, the resulting poly(OVS-DHBZ POIP) exhibited a substantial increase in performance, capturing 1.03 mmol g^{-1} of CO_2 at 298 K [Fig. 8**(b)**] and 1.68 mmol g^{-1} at 273 K. This improvement highlights the impact of thermal ROP on the material's structural and functional properties. Enhanced CO_2 capture performance can be attributed to physical and chemical adsorption mechanisms. Physical adsorption relies on the material's high surface area and porosity, whereas van der Waals forces facilitate CO_2 adsorption via a pore-filling mechanism. The increased surface area and pore volume of poly(OVS-DHBZ POIP) after thermal ROP enables more efficient pore-filling, thereby promoting greater CO_2 uptake [45]. In addition to physical adsorption, the chemical structure of poly(OVS-DHBZ POIP) plays a crucial role in enhancing interactions with CO_2 molecules. The incorporation of nitrogen (N) and hydroxyl (OH) groups into the polymer framework strengthens hydrogen bonding (OH···O═C═O) and Lewis's acid-base interactions (N$^+$···O═C═O) with CO_2 [45]. These synergistic physical and chemical adsorption processes significantly improve the material's CO_2 capture capacity, underscoring its potential for environmental and energy applications. These chemical interactions,

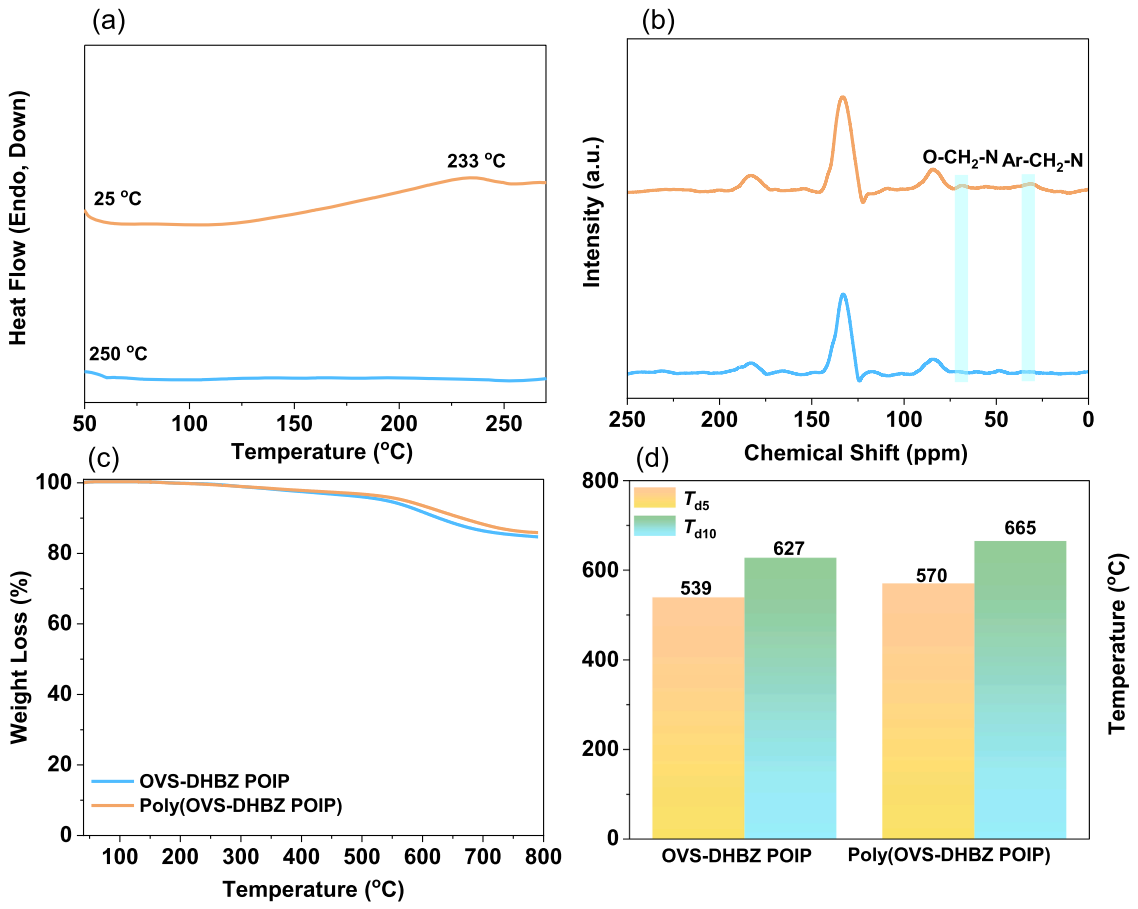

Fig. 4. (a) DSC, (b) FTIR spectra, (c) TGA analyses, and (d) char yield and T_{d10} values of OVS-DHBZ POIP monomer before and after thermal ROP.

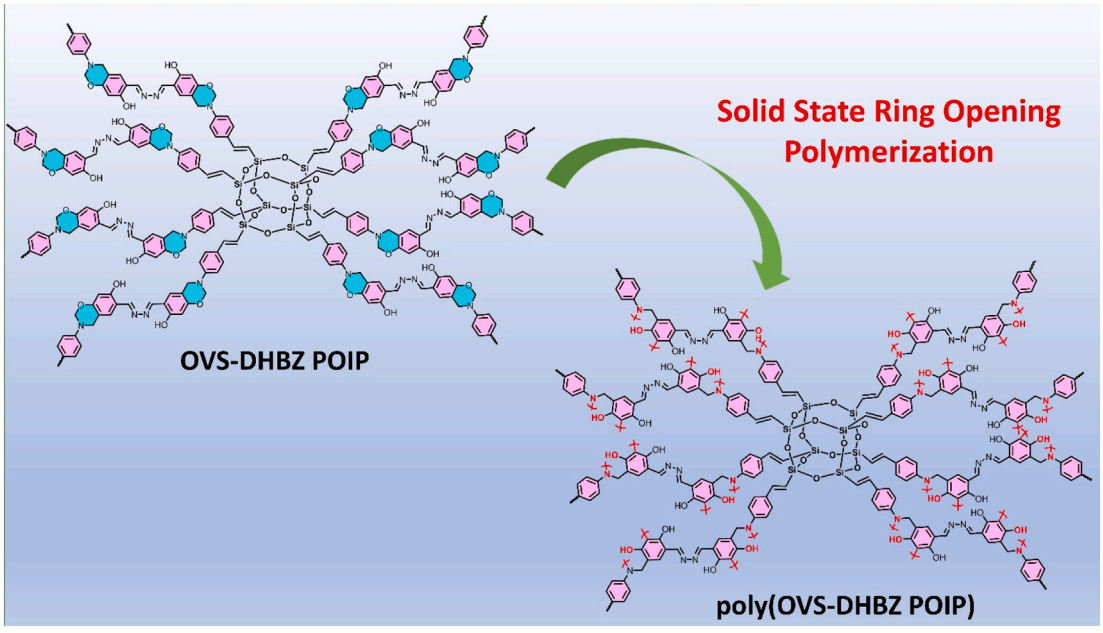

Fig. 5. Solid state thermal conversion of OVS-DHBZ POIP to form poly(OVS-DHBZ POIP).

combined with its superior physical properties, explain the improved CO_2 adsorption capacity of poly(OVS-DHBZ POIP) compared to its precursor, OVS-DHBZ POIP. The CO_2 capture capability of poly (OVS-DHBZ POIP) is superior (1.03 mmol g^{-1}) to that of other previously reported polybenzoxazines [Fig. 8**(c)**], like BoxPOP-1 (0.91 mmol g^{-1}) [35], BPOP-1 (0.67 mmol g^{-1}) [35], TPM-BZ-Py POP (0.6 mmol g^{-1}) [38] and Cr-TPA-4BZ-Py POP (0.66 mmol g^{-1}) [41]. These findings show that the poly(OVS-DHBZ POIP) may interact with CO_2

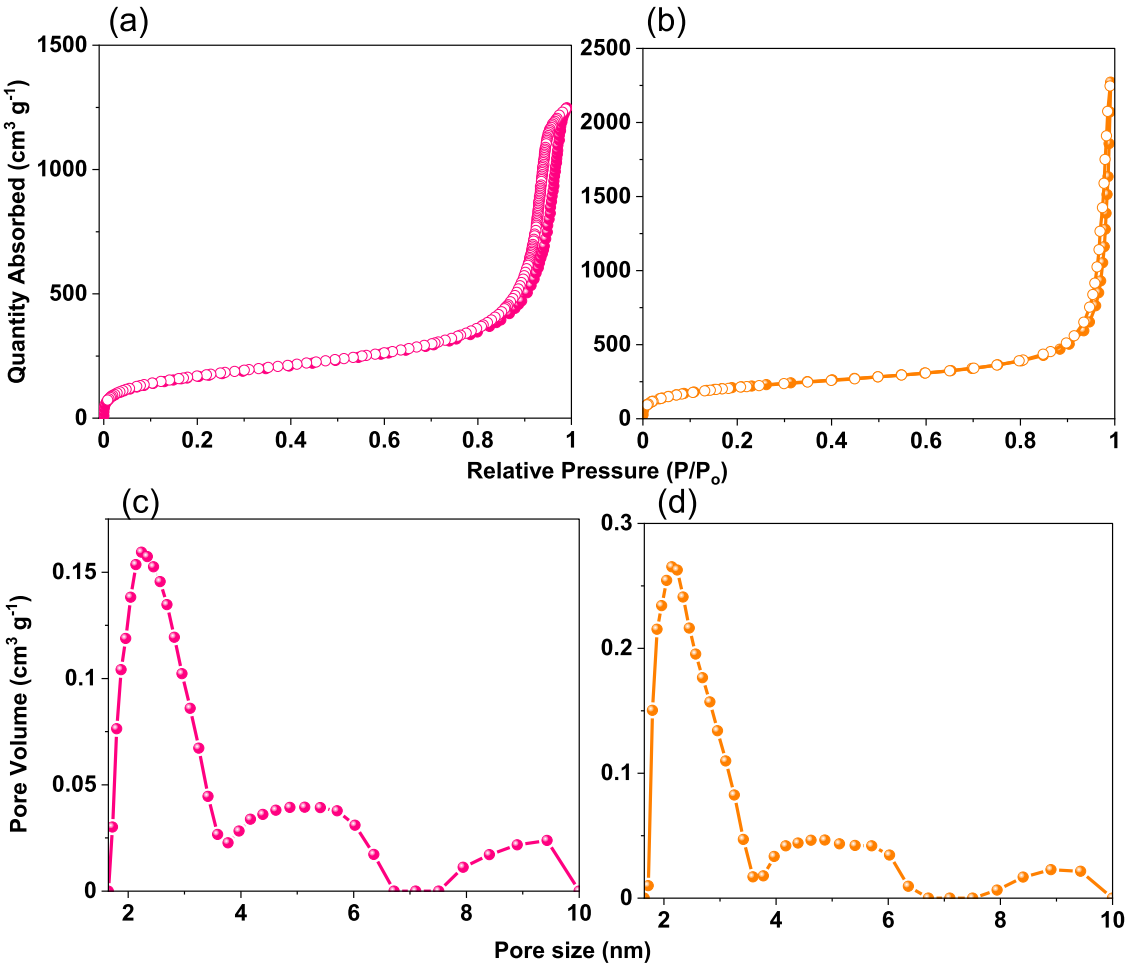

Fig. 6. (a, b) N_2 isotherms profiles and (c, d) pore diameter size of the (a, c) OVS-DHBZ POIP and (b, d) poly(OVS-DHBZ POIP).

molecules more strongly than OVS-DHBZ POIP, indicating that the inclusion of substantial N and phenolic OH units and high surface area might improve its CO_2 capture efficiency after thermal ROP.

3.5. *Electrochemical properties of OVS-DHBZ POIP and poly(OVS-DHBZ POIP)*

Porous materials are considered suitable for use as supercapacitor electrodes because they can integrate building blocks with varied properties, extensive surface areas, consistent pore diameters, and different morphologies [46–49]. We assessed the supercapacitors characteristics of our OVS-DHBZ POIP and poly(OVS-DHBZ POIP), using cyclic voltammetry (CV) and Galvanic charge-discharge (GCD) employing a three-electrode setup with 1 M aqueous KOH. [Fig. 9]. We documented the CV curves at different scan rates ranging from 5 to 200 mV s^{-1} within the potential range of 0 to −0.9 V [Fig. 9**(a) and (b)**]. The OVS-DHBZ POIP exhibited a quasi-rectangular shape across all scan rates (5 to 200 mV s^{-1}), with noticeable redox peaks, indicating both pseudocapacitance and EDLC characteristics [Fig. 9**(a)**]. The pseudocapacitance characteristics were attributed to the existence of oxygen and nitrogen groups in the OVS-DHBZ POIP [50]. After the ring-opening of the benzoxazines, the poly(OVS-DHBZ POIP) displayed a similar quasi-rectangular shape, along with the appearance of distinct oxidation (−0.59 V) and reduction (−0.66 V) peaks, suggesting enhanced pseudocapacitance characteristics compared to the original OVS-DHBZ POIP [Fig. 9**(b)**]. Following thermal ROP, hydroxyl (OH) and nitrogen (N) heteroatoms became more prominent, interacting with free electrons and contributing to an improved pseudocapacitance response. These heteroatoms facilitated efficient electron transfer by forming strong interactions with the electrolyte [51]. The CV curves of OVS-DHBZ POIP and poly(OVS-DHBZ POIP) maintained their morphology with increasing sweep rates, indicating high-rate capabilities and rapid kinetics [52,53]. Additionally, we analyzed the charge and discharge patterns, as well as the capacitances of these OVS-DHBZ POIP and poly (OVS-DHBZ POIP) at different current densities (20 A g^{-1} to 0.5 A g^{-1}) [Fig. 9**(c) and (d)**]. The GCD profiles of the poly(OVS-DHBZ POIP) exhibited a bent-triangle morphology, signifying pseudocapacitive and EDLC characteristics; this curvature resulted from the prevalence of heteroatoms [54]. In all GCD curves, the discharge duration exceeded the charging duration, indicating increased capacitance. The discharge profile of the poly(OVS-DHBZ POIP) was more pronounced than that of the OVS-DHBZ-POIP, indicating superior capacitance. The specific capacities of the OVS-DHBZ POIP (21 F g^{-1}) and poly(OVS-DHBZ POIP) (58 F g^{-1}) were determined using GCD curves, with 0.5 A g^{-1} being used for both samples [Fig. 10**(a)**]. The enhanced capacitance of the poly (OVS-DHBZ POIP) is ascribed to its high surface area, porosities, and the presence of free hydroxyl and nitrogen groups in its framework, which facilitate rapid electrolyte mobility to reach the electrode surface. At high current density (20 A g^{-1}), capacitance decreased yielding values of 5.3 F $g^{-1}$and 7.7 F g^{-1} for OVS-DHBZ POIP and poly(OVS-DHBZ POIP) respectively [Fig. 10**(a)**]. The decrease in capacitance is ascribed to the reduced diffusion time for electrolyte ions, preventing full utilization of the electrode surface for charge storage [55–57]. Furthermore, power law in **Eq. S1** was used to calculate capacitive contribution and assess the charge storage capacities of the electrodes [**Fig. S3**]. The cathodic line slopes for OVS-DHBZ POIP and poly

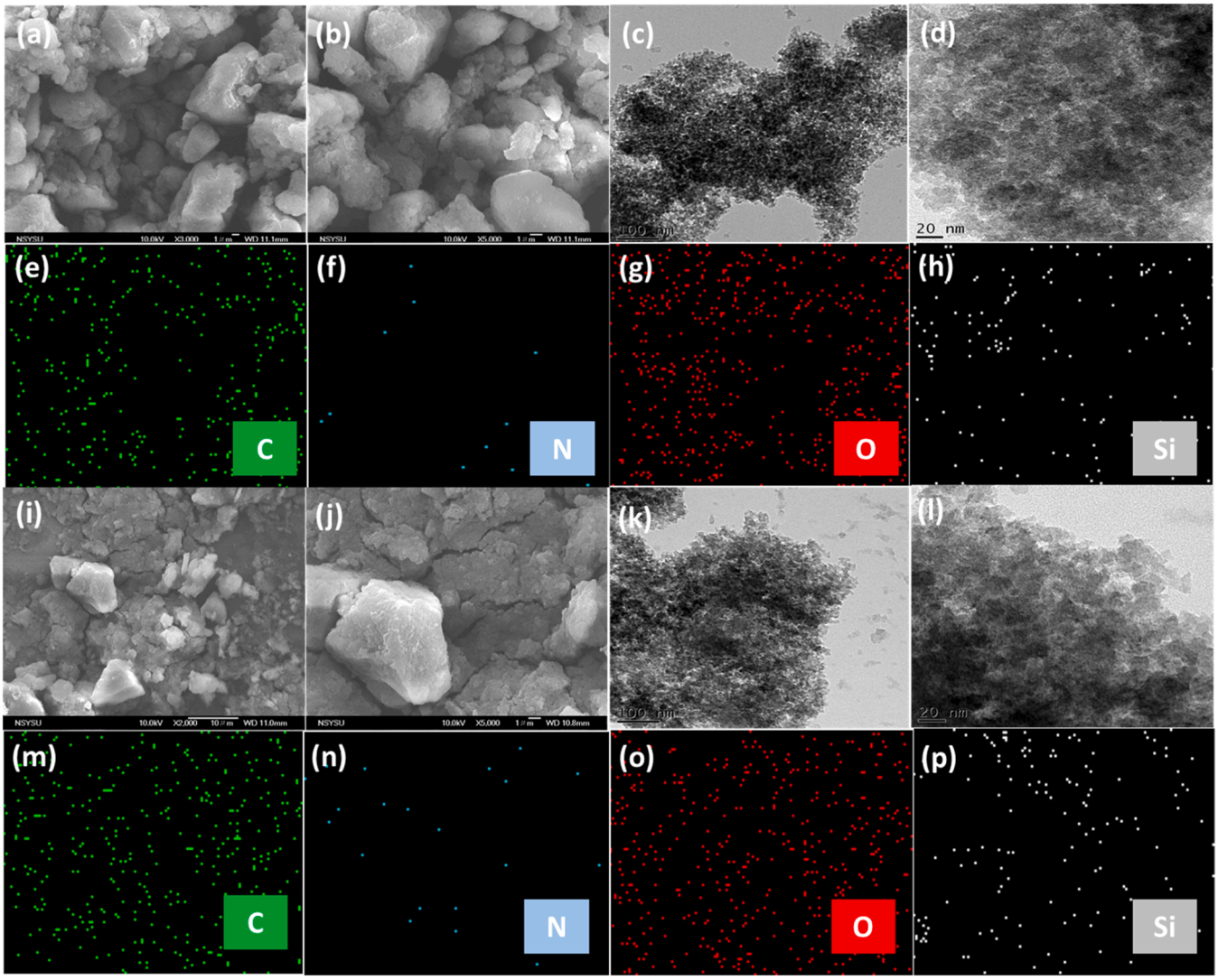

Fig. 7. (a, b) SEM images (c, d) TEM images, and (e-h) element mapping of OVS-DHBZ POIP, (i, j) SEM images (k, l) TEM images (e-h) and element mapping of poly (OVS-DHBZ POIP).

(OVS-DHBZ POIP) are computed to be 0.60, and 0.54, respectively.

The slopes of the anodic for OVS-BZ-POIP and poly(OVS-BZ-POIP) are 0.97 and 0.99, respectively (**Fig. S3**). It is common for pseudocapacitive materials to exhibit diffusion control when the slope is equal to or <0.5. But here, capacitive or surface control is mostly dominant for the charge storage mechanism. Fig. 10**(b)** illustrates the prolonged cycling resilience assessed at 1 A g^{-1} over 2000 cycles. Both of these POIPs demonstrated exceptional capacitance retention, as poly(OVS-DHBZ POIP) (97 %) outperforming the OVS-DHBZ POIP (95 %). The specific capacitance of our synthesized material's performance surpassed that of other BZ-POPs [**Table S1**]. To our knowledge, this is the first research to evaluate the potential of BZ-linked OVS for supercapacitor applications. This BZ-linked POIP looks to be an excellent candidate for energy storage systems due to its significant specific capacitance, high surface area, versatile structure, and ease of fabrication.

4. Conclusions

We successfully prepared a 3D benzoxazine-linked OVS porous organic-inorganic polymer (OVS-DHBZ POIP) using a Heck coupling reaction. The OVS-DHBZ POIP exhibited excellent properties, including high thermal stability (T_{d5} = 539 °C T_{d10} = 627 °C; char yield = 84.6 wt %), significant porosity (S_{BET} = 690 m^2/g, V_{total} = 1.98 cm^3/g), effective CO_2 capture (1.18 mmol/g at 273 K), and promising specific capacitance (21 F/g). Through solid-state thermal ROP without any curing agent, OVS-DHBZ POIP was transformed into poly(OVS-DHBZ POIP), resulting in enhanced material properties. The poly(OVS-DHBZ POIP) exhibited higher thermal stability (T_{d5} = 570 °C T_{d10} = 665 °C; char yield = 85 wt %), and porosity (S_{BET} = 762 m^2/g, V_{total} =2.3 cm^3/g), superior CO_2 capture (1.68 mmol/g at 273 K), and enhanced specific capacitance (58 F/g). The solid-state chemical transformation introduced phenolic groups and Mannich bridges, which facilitated strong intermolecular and intramolecular hydrogen bonding with guest molecules. This modification contributed to the observed improvements in thermal stability, CO_2 capture efficiency, and supercapacitor performance. This study presents a groundbreaking 3D benzoxazine-linked POIP with unique solid-state modification capabilities, making it highly suitable for gas capture and energy storage applications.

CRediT authorship contribution statement

Mohsin Ejaz: Writing – original draft, Formal analysis, Data curation, Conceptualization. **Mohamed Gamal Mohamed:** Writing – review & editing, Writing – original draft, Supervision, Methodology, Investigation, Formal analysis, Data curation, Conceptualization. **Shiao-Wei**

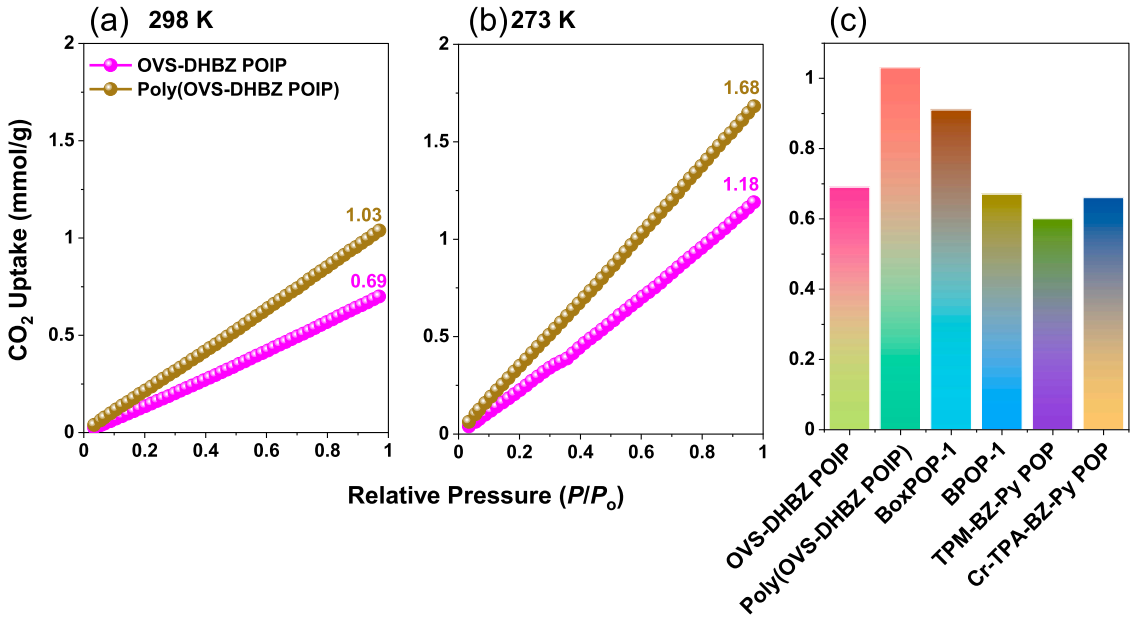

Fig. 8. CO_2 capture performance of OVS-DHBZ POIP and poly(OVS-DHBZ POIP) (a) 298 K (b) 273 K and (c) comparison of OVS-DHBZ POIP and poly(OVS-DHBZ POIP) for CO_2 uptake with reported porous PBZs.

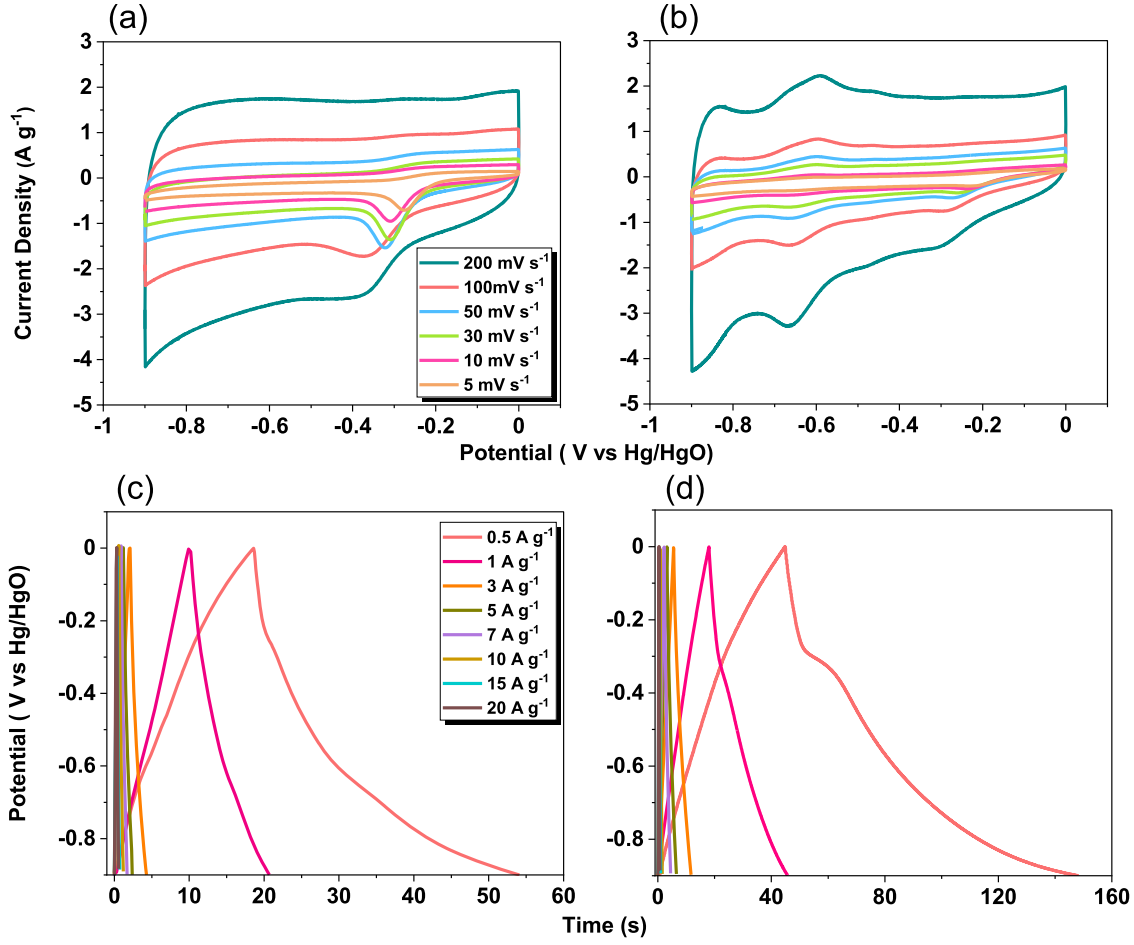

Fig. 9. (a, b) CV and (c, d) GCD curves, of (a, c) OVS-DHBZ POIP and (b, d) poly(OVS-DHBZ POIP) .

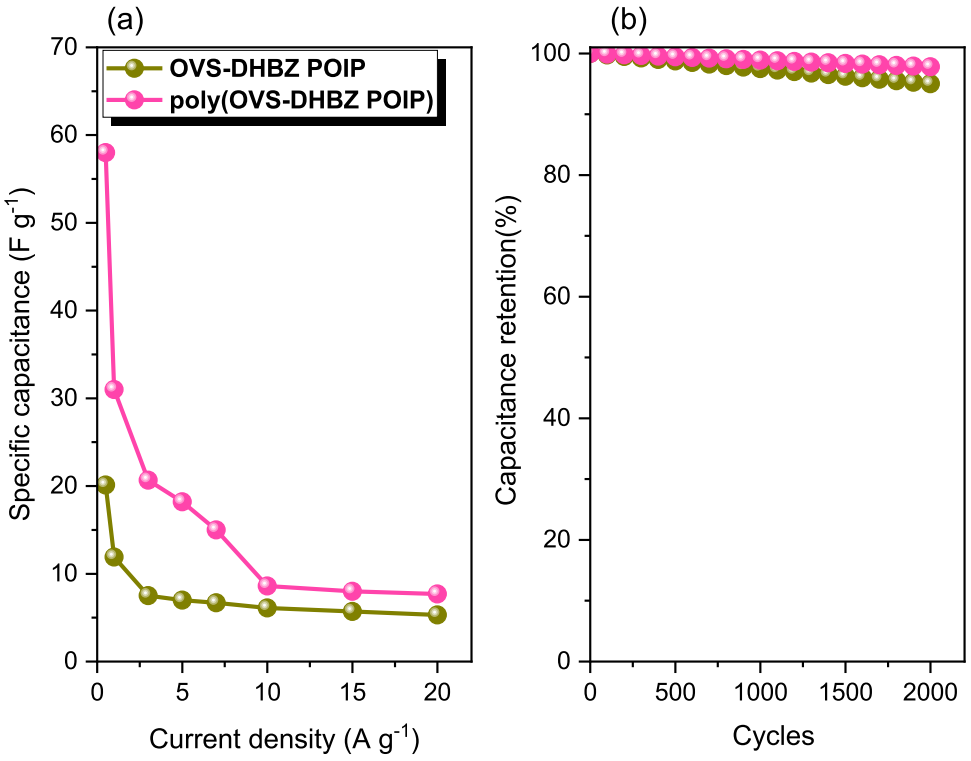

Fig. 10. (a) Specific capacitance and (b) capacitance retention profiles for OVS-DHBZ POIP and poly(OVS-DHBZ POIP).

Kuo: Supervision, Project administration, Funding acquisition.

Declaration of competing interest

The authors declare that they have no known competing financial interests or personal relationships that could have appeared to influence the work reported in this paper.

Acknowledgements

This study was supported financially by the National Science and Technology Council, Taiwan, under contracts NSTC 113-2223-E-110-001- and 113-2221-E-110-012-MY3. The authors thank the staff at National Sun Yat-sen University for their assistance with the TEM (ID: EM022600) experiments.

Supplementary materials

Supplementary material associated with this article can be found, in the online version, at doi:10.1016/j.jtice.2025.106098.

References

[1] Mohamed MG, Chen CC, Ibrahim M, Mousa AO, Elsayed MH, Ye Y, Kuo SW. Tetraphenylanthraquinone and dihydroxybenzene-tethered conjugated microporous polymer for enhanced CO_2 uptake and supercapacitive energy storage. JACS Au 2024;4:3593–605. https://doi.org/10.1021/jacsau.4c00537.

[2] Song KS, Fritz PW, Coskun A. Porous organic polymers for CO_2 capture, separation and conversion. Chem Soc Rev 2022;51:9831–52. https://doi.org/10.1039/D2CS00727D.

[3] Mohamed MG, El-Mahdy AFM, Kotp MG, Kuo SW. Advances in porous organic polymers: syntheses, structures, and diverse applications. Mater Adv 2022;3:707–33. https://doi.org/10.1039/D1MA00771H.

[4] Yang DH, Tao Y, Ding X, Han BH. Porous organic polymers for electrocatalysis. Chem Soc Rev 2022;51:761–91. https://doi.org/10.1039/D1CS00887K.

[5] Zhang Z, Jia J, Zhi Y, Ma S, Liu X. Porous organic polymers for light-driven organic transformations. Chem Soc Rev 2022;51:2444–90. https://doi.org/10.1039/D1CS00808K.

[6] Wang S, Li H, Huang H, Cao X, Chen X, Cao D. Porous organic polymers as a platform for sensing applications. Chem Soc Rev 2022;51:2031–80. https://doi.org/10.1039/D2CS00059H.

[7] Zhu Y, Xu P, Zhang X, Wu D. Emerging porous organic polymers for biomedical applications. Chem Soc Rev 2022;51:1377–414. https://doi.org/10.1039/D1CS00871D.

[8] Mousa AO, Mohamed MG, Lin ZI, Chuang CH, Chen CK, Kuo SW. Construction of cationic conjugated microporous polymers containing pyrene units through post-cationic modification for enhanced antibacterial performance. J Taiwan Inst Chem Eng 2024;157:105448. https://doi.org/10.1016/j.jtice.2024.105448.

[9] Mohamed MG, Elewa AM, Li MS, Kuo SW. Construction and multifunctional of hypercrosslinked porous organic polymers containing ferrocene unit for high-performance iodine adsorption and supercapacitor. J Taiwan Inst Chem Eng 2023;150:105045. https://doi.org/10.1039/D1CS01014J.

[10] Sun H, Li J, Liang W, Gong X, Jing A, Yang W, Liu H, Ren S. Porous organic polymers as active electrode materials for energy storage applications. Small Methods 2024;8:2301335. https://doi.org/10.1002/smtd.202301335.

[11] Lin X, Deng Y-Y, Zhang Q, Han D, Fu Q. Effect of POSS size on the porosity and adsorption performance of hybrid porous polymers. Macromolecules 2023;56:1243–52. https://doi.org/10.1021/acs.macromol.2c02486.

[12] Chen G, Zhang Y, Xu J, Liu X, Liu K, Tong M, Long Z. Imidazolium-based ionic porous hybrid polymers with POSS-derived silanols for efficient heterogeneous catalytic CO_2 conversion under mild conditions. Chem Eng J 2020;381:122765. https://doi.org/10.1016/j.cej.2019.122765.

[13] Mohamed MG, Tsai MY, Wang CF, Huang CF, Danko M, Dai L, Chen T, Kuo SW. Multifunctional polyhedral oligomeric silsesquioxane (POSS) based hybrid porous materials for CO_2 uptake and iodine adsorption. Polymers 2021;13:221. https://doi.org/10.3390/polym13020221.

[14] Mohamed MG, Kuo SW. Progress in the self-assembly of organic/inorganic polyhedral oligomeric silsesquioxane (POSS) hybrids. Soft Matter 2022;18:5535–61. https://doi.org/10.1039/D2SM00635A.

[15] Ejaz M, Samy MM, Ye Y, Kuo SW, Mohamed MG. Design hybrid porous organic/inorganic polymers containing polyhedral oligomeric silsesquioxane/pyrene/anthracene moieties as a high-performance electrode for supercapacitor. Int J Mol Sci 2023;24:2501. https://doi.org/10.3390/ijms24032501.

[16] Mohamed MG, Elsayed MH, Ye Y, Samy MM, Hassan AE, Mansoure TH, Wen Z, Chou HH, Chen KH, Kuo SW. Construction of porous organic/inorganic hybrid polymers based on polyhedral oligomeric silsesquioxane for energy storage and hydrogen production from water. Polymers 2023;15:182. https://doi.org/10.3390/polym15010182.

[17] Mohamed MG, Hammad Elsayed M, Hassan AE, Basit A, Mekhemer IMA, Chou HH, Chen KH, Kuo SW. Hybrid porous polymers combination of octavinylsilsesquioxane/pyrene with benzothiadiazole units for robust energy storage and efficient photocatalytic hydrogen production from water. ACS Appl Polym Mater 2024;6:5945–56. https://doi.org/10.1021/acsapm.4c00655.

[18] Ejaz M, Mohamed MG, Sharma SU, Lee JT, Huang CF, Chen T, Kuo SW. An ultrastable porous polyhedral oligomeric silsesquioxane/tetraphenylthiophene

hybrid as a high-performance electrode for supercapacitors. Molecules 2022;27:6238. https://doi.org/10.3390/molecules27196238.
[19] Hsiao CW, Elewa AM, Mohamed MG, Kuo SW. Highly stable hybrid porous polymers containing polyhedral oligomeric silsesquioxane (POSS)/dibenzo[g,p]chrysene and dibenzo[b,d]thiophene units for efficient Rhodamine B dye removal. Sep Purif Technol 2024;332:125771. https://doi.org/10.1016/j.seppur.2023.125771.
[20] Wang H, Hang G, Hu J, Gao Y, Li L, Zheng S. Organic–Inorganic polyimides with POSS cages in the main chains: an impact of POSS R groups on morphologies and properties. ACS Appl Polym Mater 2023;5:4274–87. https://doi.org/10.1021/acsapm.3c00456.
[21] Wang D, Yang W, Li L, Zhao X, Feng S, Liu H. Hybrid networks constructed from tetrahedral silicon-centered precursors and cubic POSS-based building blocks via Heck reaction: porosity, gas sorption, and luminescence. J Mater Chem A 2013;1:13549–58. https://doi.org/10.1039/C3TA12324C.
[22] Ejaz M, Mohamed MG, Chen YT, Zhang K, Kuo SW. Porous carbon materials augmented with heteroatoms derived from hyperbranched biobased benzoxazine resins for enhanced CO_2 adsorption and exceptional supercapacitor performance. J Energy Storage 2024;78:110166. https://doi.org/10.1016/j.est.2023.110166.
[23] Basit A, Mohamed MG, Sharma SU, Kuo SW. Thianthrene- and Thianthrene tetraoxide-functionalized conjugated microporous polymers for efficient energy storage. ACS Appl Polym Mater 2024;6:12247–60. https://doi.org/10.1021/acsapm.4c02368.
[24] Cheng H, Li J, Meng T, Shu D. Advances in Mn-based MOFs and their derivatives for high-performance supercapacitor. Small 2024;20:2308804. https://doi.org/10.1002/smll.202308804.
[25] Molahalli V, K C, Singh MK, Agrawal M, Krishnan SG, Hegde G. Past decade of supercapacitor research – Lessons learned for future innovations. J Energy Storage 2023;70:108062. https://doi.org/10.1016/j.est.2023.108062.
[26] Pandey D, Kumar KS, Thomas J. Supercapacitor electrode energetics and mechanism of operation: uncovering the voltage window. Prog Mater Sci 2024;141:101219. https://doi.org/10.1016/j.pmatsci.2023.101219.
[27] Samy MM, Mohamed MG, Kuo SW. Pyrene-functionalized tetraphenylethylene polybenzoxazine for dispersing single-walled carbon nanotubes and energy storage. Compos Sci Technol 2020;199:108360. https://doi.org/10.1016/j.compscitech.2020.108360.
[28] Samy MM, Mohamed MG, Kuo SW. Directly synthesized nitrogen-and-oxygen–doped microporous carbons derived from a bio-derived polybenzoxazine exhibiting high-performance supercapacitance and CO_2 uptake. Eur Polym J 2020;138:109954. https://doi.org/10.1016/j.eurpolymj.2020.109954.
[29] Chen CY, Chen WC, Mohamed MG, Chen ZY, Kuo SW. Highly thermally stable, reversible, and flexible main chain type benzoxazine hybrid incorporating both polydimethylsiloxane and double-decker shaped polyhedral silsesquioxane units through diels–Alder reaction. Macromol Rapid Commun 2023;44:2200910. https://doi.org/10.1002/marc.202200910.
[30] Mohamed MG, Li C-J, Khan MAR, Liaw CC, Zhang K, Kuo SW. Formaldehyde-free synthesis of fully Bio-based multifunctional bisbenzoxazine resins from natural renewable starting materials. Macromolecules 2022;55:3106–15. https://doi.org/10.1021/acs.macromol.2c00417.
[31] Aly KI, Ebrahium SM, Abdelhamid HN, El-Bery HM, Mohammed AAK, Huang CW, Mohamed MG. Efficient synthesis of main chain thermosetting polybenzoxazine resin containing tert-butylcyclohexanone and diphenylmethane units for supercapacitor energy storage. Eur Polym J 2024;221:113519. https://doi.org/10.1016/j.eurpolymj.2024.113519.
[32] Mukherjee S, Lochab B. Hydrogen bonding-guided strategies for thermal performance modulation in biobased oxazine ring-substituted benzoxazine thermosets. Macromolecules 2024;57:1795–807. https://doi.org/10.1021/acs.macromol.3c02454.
[33] Yang R, Yang R, Yang S, Zhang K. Hydrogen bonding-rich bio-benzoxazine resin provides high-performance thermosets and ultrahigh-performance composites. ACS Sustain Chem Eng 2024;12:1728–39. https://doi.org/10.1021/acssuschemeng.3c07460.
[34] Ejaz M, Mohamed MG, Kuo SW. Solid state chemical transformation provides a fully benzoxazine-linked porous organic polymer displaying enhanced CO_2 capture and supercapacitor performance. Polym Chem 2023;14:2494–509. https://doi.org/10.1039/D3PY00158J.
[35] Xu S, He J, Jin S, Tan B. Heteroatom-rich porous organic polymers constructed by benzoxazine linkage with high carbon dioxide adsorption affinity. J Colloid Interface Sci 2018;509:457–62. https://doi.org/10.1016/j.jcis.2017.09.009.
[36] Mohamed MG, Chen TC, Kuo SW. Solid-State chemical transformations to enhance gas capture in benzoxazine-linked conjugated microporous polymers. Macromolecules 2021;54:5866–77. https://doi.org/10.1021/acs.macromol.1c00736.
[37] Sun X, Li J, Wang W, Ma Q. Constructing benzoxazine-containing porous organic polymers for carbon dioxide and hydrogen sorption. Eur Polym J 2018;107:89–95. https://doi.org/10.1016/j.eurpolymj.2018.07.043.
[38] Mohamed MG, Chen CC, Zhang K, Kuo SW. Construction of three-dimensional porous organic polymers with enhanced CO_2 uptake performance via solid-state thermal conversion from tetrahedral benzoxazine-linked precursor. Eur Polym J 2023;200:112551. https://doi.org/10.1016/j.eurpolymj.2023.112551.
[39] Mohamed MG, Lin R-C, Tu J-H, Lu F-H, Hong J-L, Jeong K-U, Wang C-F, Kuo S-W. Thermal property of an aggregation-induced emission fluorophore that forms metal–ligand complexes with $Zn(ClO_4)_2$ of salicylaldehyde azine-functionalized polybenzoxazine. RSC Adv 2015;5:65635–45. https://doi.org/10.1039/C5RA09409G.
[40] Mohamed MG, Chang W-C, Kuo SW. Crown ether- and benzoxazine-linked porous organic polymers displaying enhanced metal ion and CO_2 capture through solid-State chemical transformation. Macromolecules 2022;55:7879–92. https://doi.org/10.1021/acs.macromol.2c01216.
[41] Mohamed MG, Su BX, Kuo SW. Robust nitrogen-doped microporous carbon via crown ether-functionalized benzoxazine-linked porous organic polymers for enhanced CO_2 adsorption and supercapacitor applications. ACS Appl Mater Interfaces 2024;16:40858–72. https://doi.org/10.1021/acsami.4c05645.
[42] Ejaz M, Mohamed MG, Kuo SW. Fluorescent benzoxazine–Perylene linked covalent organic polymer as a sensing probe for lead ions and 2,4,6-trinitrophenol. ACS Appl Polym Mater 2024;6:9170–9. https://doi.org/10.1021/acsapm.4c01514.
[43] Mohamed MG, Mansoure TH, Takashi Y, Samy MM, Chen T, Kuo SW. Ultrastable porous organic/inorganic polymers based on polyhedral oligomeric silsesquioxane (POSS) hybrids exhibiting high performance for thermal property and energy storage. Micropor Mesopor Mater 2021;328:111505. https://doi.org/10.1016/j.micromeso.2021.111505.
[44] Elewa AM. Hydrogen-bonded organic frameworks (HOFs) from design to environmental application. J Ind Eng Chem 2024. https://doi.org/10.1016/j.jiec.2024.11.002.
[45] Gao X, Yang S, Hu L, Cai S, Wu L, Kawi S. Carbonaceous materials as adsorbents for CO_2 capture: synthesis and modification. Carbon Capture Sci Technol 2022;3:100039. https://doi.org/10.1016/j.ccst.2022.100039.
[46] Zhai Z, Zhang L, Du T, Ren B, Xu Y, Wang S, Miao J, Liu Z. A review of carbon materials for supercapacitors. Mater Des 2022;221:111017. https://doi.org/10.1016/j.matdes.2022.111017.
[47] Sun L, Gong Y, Li D, Pan C. Biomass-derived porous carbon materials: synthesis, designing, and applications for supercapacitors. Green Chem 2022;24:3864–94. https://doi.org/10.1039/D2GC00099G.
[48] Jiang G, Senthil RA, Sun Y, Kumar TR, Pan J. Recent progress on porous carbon and its derivatives from plants as advanced electrode materials for supercapacitors. J Pow Sour 2022;520:230886. https://doi.org/10.1016/j.jpowsour.2021.230886.
[49] Chandra Mouli KVV, Kalla RMN, Ramachandran T, Kumar YA, Moniruzzaman M, Lee J. Cutting-edge advancements in HOFs-derived materials for energy storage supercapacitor application. Int J Hydrogen Energy 2024;90:1–24. https://doi.org/10.1016/j.ijhydene.2024.09.419.
[50] Zhu W, Shen D, Xie H. Effect of heteroatoms on pseudocapacitance for N/O Co-doped porous carbon in an alkaline aqueous electrolyte. Energy Fuels 2023;37:12467–73. https://doi.org/10.1021/acs.energyfuels.3c02061.
[51] Liu K, Yu C, Xie Y, Guo W, Yu J, Ni L, Wang Z, Fu R, Qiu J. Correlation between self-discharge behavior and heteroatoms over doped carbon sheets for enhanced pseudocapacitance. J Energy Chem 2022;72:291–8. https://doi.org/10.1016/j.jechem.2022.05.004.
[52] Basit A, Kao YC, El-Ossaily YA, Kuo SW, Mohamed MG. Rational engineering and synthesis of pyrene and thiazolo[5,4-d]thiazole-functionalized conjugated microporous polymers for efficient supercapacitor energy storage. J Mater Chem A. 2024;12:30508–21. https://doi.org/10.1039/D4TA05908E.
[53] Samy MM, Mohamed MG, Sharma SU, Chaganti SV, Lee JT, Kuo SW. An ultrastable tetrabenzonaphthalene-linked conjugated microporous polymer functioning as a high-performance electrode for supercapacitors. J Taiwan Inst Chem Eng 2024;(158):104750. https://doi.org/10.1016/j.jtice.2023.104750.
[54] Gopalakrishnan A, Badhulika S. Effect of self-doped heteroatoms on the performance of biomass-derived carbon for supercapacitor applications. J Pow Sour 2020;480:228830. https://doi.org/10.1016/j.jpowsour.2020.228830.
[55] S.V. Chaganti, S.U. Sharma, M. Ibrahim, A. Basit, P.N. Singh, S.W. Kuo, M.G. Mohamed, Redox-active a pyrene-4,5,9,10-tetraone and thienyltriazine-based conjugated microporous polymers for boosting faradaic supercapacitor energy storage, J Pow Sour 627 (2025) 235848. https://doi.org/10.1016/j.jpowsour.2024.235848.
[56] Mohamed MG, Kotp MG, Mousa AO, Li YS, Kuo SW. Construction of Fe- and N-doped microporous carbon from ferrocene-based conjugated microporous polymers for supercapacitive energy storage. ACS Appl Energy Mater 2025. https://doi.org/10.1021/acsaem.4c02968.
[57] Mousa AO, Sharma SU, Chaganti SV, Mansoure TH, Singh PN, Ejaz M, Chuang CH, Lee JT, Kuo SW, Mohamed MG. Designing strategically functionalized conjugated microporous polymers with pyrene and perylenetetracarboxylic dianhydride moieties with single-walled carbon nanotubes to enhance supercapacitive energy storage efficiency. J Pow Sour 2024;608:234624. https://doi.org/10.1016/j.jpowsour.2024.234624.